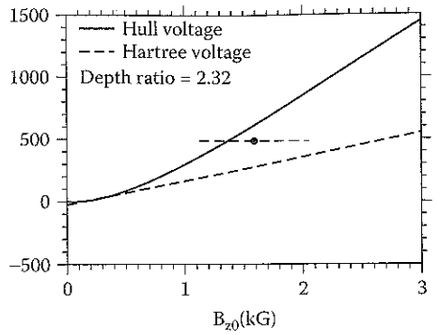

FIGURE 7.32
Operating space for the π-mode (n = 7) in a rising-sun magnetron with N = 14, r_c = 7.3 cm, r_{a1} = 12.5, r_{a2} = 16.2 cm, and cathode length L_c = 20.8 cm, with an operating frequency of 1.052 GHz. (From Lemke, R.W. et al., *Phys. Plasmas*, 7, 706, 2000. With permission.)

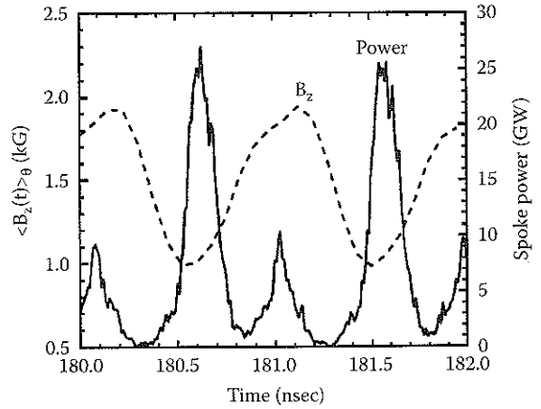

FIGURE 7.33
The spoke power incident on the anode (solid curve) and B_z averaged over θ, which recovers both the static applied field and the time-dependent 0-harmonic component. (From Lemke, R.W. et al., *Phys. Plasmas*, 7, 706, 2000. With permission.)

of the RF magnetic field cancels the applied magnetic field, thus showing the effect of losing insulation for that brief period.

We estimate the limiting condition on the RF magnetic field magnitude B_{RF} as follows:

$$\Delta B_{RF} \le \frac{1}{2}\left(B^M - B^*\right) \tag{7.25}$$

where B^M is the applied axial magnetic field for maximum power output, as illustrated by the dot in Figure 7.32, slightly less than the Buneman–Hartree field B_{BH}. Since the total power available, proportional to B_{RF}, is proportional to the square of the separation between the Buneman–Hartree and Hull fields, this condition indicates that high power operation occurs at the high-field end of the Buneman–Hartree condition, i.e., high B_z and voltage. Palevsky and Bekefi[8] and Ballard[52] have shown that the A6 magnetron operating in the 2π-mode is limited by this condition to an RF electric field of 750 kV/cm, or an operating power of 3 GW.

Young[28] has derived a non-linear magnetron model that predicts a saturated power level of

$$P_{sat} = \frac{\omega_n}{Q_L} W_{NL}\left(1 - X\right) \tag{7.26}$$

where W_{NL} is the saturation level of wave energy and $X = \omega_n/2Q_L\Omega$, where Q_L is the loaded Q of the magnetron and Ω is the instability growth rate, taken by Young to be the magnetron instability growth rate:

$$\Omega = \frac{\omega_c}{16} \tag{7.27}$$

with ω_c the cyclotron frequency. W_{NL} can be expressed in terms of the RF magnetic field energy integrated over the volume of the interaction region, and thus Young's analysis can be compared directly with predictions of Equation 7.25. Sze and coworkers compared the above analysis with A6 performance[28] and found good agreement between Equation 7.26 and experimental results. Note that Equation 7.26 implies an optimum at $Q_L = \omega_n/\Omega$. No experimental work to optimize Q values has been attempted other than Sze's multiple-waveguide extraction experiment. Because $P \sim (B_{RF})^2 V_{res}$, where V_{res} is the resonator volume, $P \sim \lambda^2$, which has been verified experimentally.[16]

Because there is an apparent upper limit on the RF power from a single magnetron, and because pulse duration limits are not yet fully mastered, the total energy presently extracted from single relativistic magnetrons is typically tens of joules, with the exception of the one experiment of the Tomsk group in the Soviet Union,[53] which reported 140 J. Since many applications will require large radiated energies, magnetron research will focus on extension of the pulse duration and on grouping magnetrons together to radiate in phase.

7.6.2 Efficiency Limits

Conventional magnetron efficiency increased steadily from its original development at low efficiencies to contemporary 80 to 90% efficiency in optimized designs. The relativistic magnetron at this phase of its development has achieved values of a few tens of percent. Values as high as 40% have been

reported. Because the total extracted power is a product of multiple factors, as shown in Equations 7.21 and 7.22, most notably the electronic efficiency, the effectiveness in minimizing the axial current, and the efficiencies of extraction, mode conversion (if included), and radiation from the antenna, it is difficult to isolate the limiting physical factors.

Ballard has estimated an upper limit on the electronic efficiency η_e.[29] In arriving at the anode, the portion of the DC potential that has not been converted into RF energy appears as kinetic energy deposited in the anode block. Therefore,

$$\eta_e = 1 - \frac{\left(<\gamma_a> -1\right)mc^2}{eV} \tag{7.28}$$

with $<\gamma_a>$ the average relativistic factor for electrons striking the anode. Slater provided a conservative, nonrelativistic estimate of the kinetic energy of the electrons striking the anode by assuming that in the worst case their velocity on impact was the sum of the $\mathbf{E} \times \mathbf{B}$ drift velocity and a Larmor rotation velocity component aligned with it,[54] arriving at

$$\eta_e^{nr} = 1 - \frac{2V^*}{A^{*2}} \tag{7.29}$$

Ballard generalized that expression to relativistic energies, estimating $<\gamma_a>$ to find

$$\eta_e = 1 - \frac{2V^*}{A^{*2} - V^{*2}} \tag{7.30}$$

where

$$V^* = \frac{eV}{mc^2}, \quad A^* = \frac{eB_z}{mc} d_e \tag{7.31}$$

Comparing Equations 7.29 and 7.30 shows that the maximum possible efficiency is always larger in the nonrelativistic case.

Ballard's expression, Equation 7.30, is compared to the experimental data[14] in Figure 7.34. Clearly, experimental efficiencies are lower than the theoretical maximum, typically by a factor of two or more. Within the magnetron itself, one of the major issues is the axial loss of electrons, as described in Equation 7.22. Loss from the cathode tip can be minimized, but when the axial current in the magnetron is large, there is a substantial $E_r \times B_\theta$ drift in the axial direction that flushes electrons from the resonator before they can produce

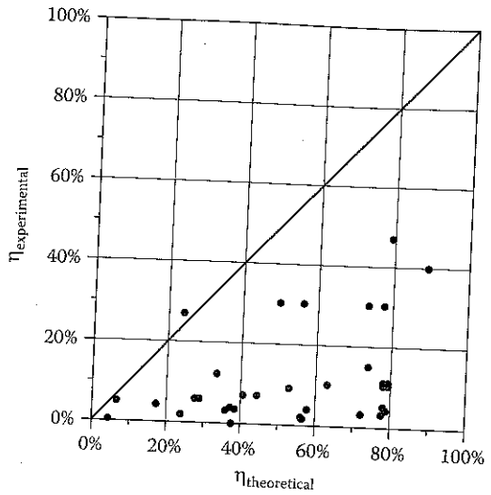

FIGURE 7.34
Comparison of theoretical efficiency, from Equation 7.30, and experimentally observed efficiencies. (From Treado, T., Generation and Diagnosis of Long- and Short-Pulse, High-Power Microwave Radiation from Relativistic Rising-Sun and A6 Magnetrons, Ph.D. thesis, University of North Carolina, Chapel Hill, 1989. With permission.)

high power. The condition that guarantees that electrons have sufficient time to interact with the anode structure before drifting axially out of the anode block is

$$\tau_\theta \le \tau_z \tag{7.32}$$

with τ_θ the circumferential transit time and τ_z the longitudinal transit time. Since both drifts are due to $E \times B$ forces, this relation becomes, in practical units,

$$I(kA) \le 0.08 B_z(T) h(cm) \tag{7.33}$$

with h the axial length of the magnetron. For example, in the A6 magnetron, at 0.45 T, the predicted threshold is 24 kA, and the threshold observed by Benford et al.[17] is 15 to 20 kA. The rapid drop in power with increasing axial current at fixed magnetic field shown in Figure 7.30 illustrates the effect. The result is that there is effectively a lower bound on the impedance at which a relativistic magnetron can operate. Combining Equation 7.33 with Equation 7.8 requires $Z > 16\ \Omega$ for an S-band magnetron. Lovelace and Young derived Equation 7.9 to account for axial current flow, and limited experimental data indicate that this condition is followed for high power operation.[17]

Additional explanations for the lower efficiencies seen in Figure 7.34 include two others we have already discussed: possibly suboptimal extraction methods, a topic that has not yet been fully explored, and downstream efficiency issues with antenna coupling and, if included, mode conversion. In addition, we speculate that nonlinear interactions with electrode plasmas dissipate energy, although these interactions are not yet understood. Finally, resonators may not be optimally designed at this stage, just as conventional magnetrons were nonoptimal in their initial embodiments.

7.6.3 Frequency Limits

The two sets of experiments with X-band magnetrons indicate that magnetrons do not scale well to higher frequencies.[30,31] In the experiments, the efficiency was relatively poor, and given the small size of the device, anode damage severely limited the lifetime. Another drawback is the scaling of the magnetic field with wavelength or frequency, which pushes the magnetic field requirement up. To see this, consider the Buneman–Hartree relation, which we rewrite in the form

$$V_{BH} = \frac{\pi B_{BH} r_a^2}{n\lambda}\left(1-\frac{r_c^2}{r_a^2}\right) - \frac{mc^2}{e}\left(1-\sqrt{1-\beta_{ph}^2}\right) \tag{7.34}$$

where $v_{ph} = r_a\omega_n/n$ is the azimuthal rotation velocity of the operating mode of the magnetron and $\beta_{ph} = v_{ph}/c$. Provided the far right term in parentheses is small compared to the first term, and given that π/n is of order unity, we can write

$$V_{BH} \sim \frac{B_{BH} r_a^2}{\lambda}\left(1-\frac{r_c^2}{r_a^2}\right) \tag{7.35}$$

Therefore, for constant voltage and radial aspect ratio,

$$\frac{B_{BH} r_a^2}{\lambda} \sim \text{constant} \tag{7.36}$$

Now, since $r_a \sim \lambda$, $B_{BH} \propto 1/\lambda$, so for a fixed voltage, higher magnetic fields are required at high frequencies, while the anode block becomes smaller. Gap alignment becomes more difficult, and heating and anode erosion become more substantial. The X-band radiator is already quite small (see Figure 7.8), making extrapolation to shorter wavelengths doubtful.

7.7 MILOs

The *magnetically insulated line oscillator* (MILO) is essentially a linear magnetron that takes advantage of a property of very high power transmission lines: at high voltages, electrons are emitted from the cathode side of the line, but the current carried creates a sufficiently strong magnetic field that these electrons cannot cross the gap. Thus, these lines are self-insulated, and the electrons drift axially in the crossed electric and self-magnetic fields.

In the MILO, a slow-wave structure is added to the anode side of the line, so that the axially drifting electrons in the layer adjacent to the cathode side interact with the axially directed slow electromagnetic wave to generate microwaves. MILOs can have either coaxial or planar geometry. In the cylindrical form, the electric field is radial, the magnetic field is azimuthal, and electron drift is axial. For magnetic insulation to occur, the axial current I_z must exceed the so-called *parapotential current*:[55]

$$I_z > I_p(A) = 8500\gamma G \ell n\left(\gamma + \sqrt{\gamma^2 - 1}\right) \tag{7.37}$$

where γ is as defined in Equation 7.6 and G is a geometric factor equal to $[\ell n(b/a)]^{-1}$ for coaxial cylinders of inner and outer radii b and a, and equal to $W/2\pi d$ for parallel plates of width W separated by gap d (see Problem 14). Because I_p is roughly proportional to γ, the logarithmic term on the right of Equation 7.37 being rather weak, the upper limit on the impedance of a magnetically insulated line is almost independent of voltage: $Z_p = V/I_p \approx 52G^{-1}\ \Omega$ for voltages around 1 MV. A MILO must have a load impedance, such as a diode, in order to establish insulation; if the load current is too small, enough current will flow across the line upstream of the load to reach the value in Equation 7.37. In this regard, Equation 7.37 is the MILO's version of the Hull condition in Equation 7.5 for magnetrons.

Because the magnetic and electric fields both arise from the pulsed power source, their ratio is also a weak function of voltage. The axial drift velocity of electrons is

$$\frac{v_d}{c} = \frac{Z_p}{Z_0} \tag{7.38}$$

where Z_0 is the transmission line impedance in the absence of magnetically insulated electron flow (see Problems 15 and 16). Because the drift velocity is proportional to Z_p, which is almost independent of voltage, the MILO naturally operates at constant drift velocity, and therefore has none of the tuning requirements of the magnetron. The magnetic field automatically

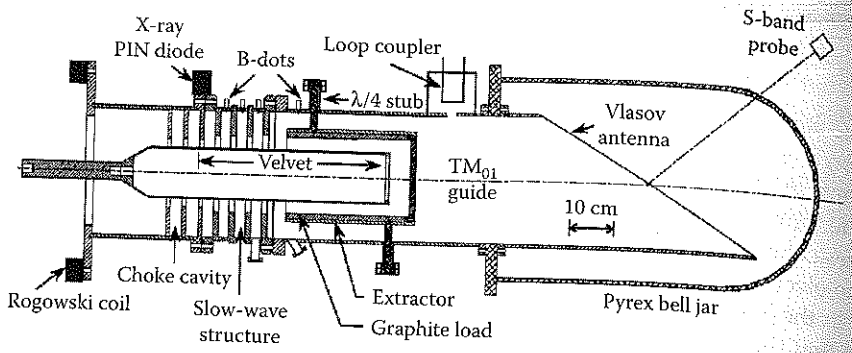

FIGURE 7.35
The cylindrical Hard-Tube MILO of Haworth et al. (From Haworth, M.D. et al., *IEEE Trans. Plasma Sci.*, 26, 312, 1998. With permission.)

adjusts to changing drive voltage, maintaining constant drift velocity.* Another key practical aspect of the MILO is that the insulating magnetic field is created without the aid of external coils, allowing the elimination of the magnets, their power supply, and any cooling required, and facilitating designs with large cross-sectional areas.

MILO development has proceeded along two major lines. One group is working to optimize a design such as that shown in Figure 7.35,[56] which has been called the *Hard-Tube MILO* (HTMILO). Within this MILO, electrons are emitted from the velvet-covered cathode of 11.43 cm diameter; the velvet speeds the turn-on of the MILO by reducing the emission field at the cathode and making emission more uniform. The outer conductor on the anode side, which comprises the base of the device cavities and the outer wall of the extractor section, has a diameter of 28.575 cm. The role of the two leftmost choke cavities, which are bounded by three vanes of inner diameter 15.24 cm and are thus somewhat deeper than those of the MILO section to their right, is to reflect microwaves back into the MILO section, rather than letting them travel upstream into the pulsed power. Additionally, the impedance mismatch between the choke and MILO sections creates a higher downstream current. The vanes in the four-cavity slow-wave structure have an inner diameter of 17.145 cm, except for the rightmost vane, which functions as a transition into the coaxial extractor section; this vane has an inner diameter of 17.780 cm. The period of all vanes is 3.81 cm. The 28.575-cm outer conductor and a 20.955-cm-diameter inner conductor bound the coaxial extraction section. The velvet-covered cathode and the graphite-coated inner surface of the extractor section form the 500-kV, 60-kA magnetically insulated transmission line (MITL) that carries the insulating current. Microwaves are extracted first into a TM_{01} waveguide and then out through a Vlasov antenna and Pyrex bell-jar radome that supports a base vacuum in

* Because of space-charge forces, there is radial variation in v_d, so lack of tuning sensitivity is only true to the first order, but is observed experimentally.

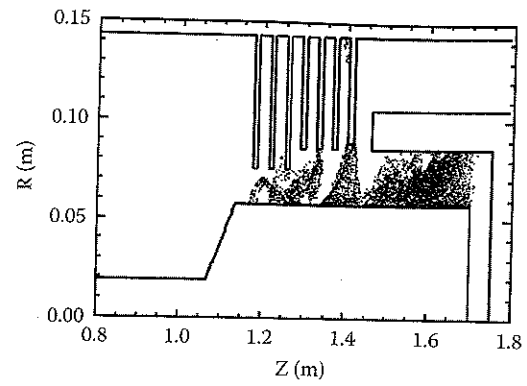

FIGURE 7.36
Electron spoke formation in the HTMILO from simulations with the 2-dimensional particle-in-cell code TWOQUICK. (From Haworth, M.D. et al., *IEEE Trans. Plasma Sci.*, 26, 312, 1998. With permission.)

the device of about 3×10^{-6} torr. The Rogowski coil measures current into the device from the 500-kV, 50-Ω, 300-nsec pulsed power system, the x-ray PIN diodes detect the bremsstrahlung radiation from energetic electrons lost on the vanes, the B-dot probes are used to measure the current at different locations, and the S-band probe is used because its reduced coupling to the 1.2-GHz L-band output is required by the high power levels to which it is exposed. Computer simulation of the HTMILO[56] (Figure 7.36) shows spoke formation characteristic of π-mode operation, which is to be expected in devices that are essentially linear magnetrons.

The process by which this group has improved upon its MILO design illustrates the range of improvements, from obvious to subtle, required to iteratively optimize a device. The device in Figure 7.35 incorporated several design improvements over a 1.5-GW, 70-nsec design described 3 years earlier[57] that were meant to improve both power and pulse length: (1) finger-stock RF joints in the earlier device were replaced with all-stainless-steel brazed construction; (2) the supports of the extractor section were quarter-wavelength stubs, rather than support rods making gravity contact with the extractor; and (3) the operating base pressure was reduced by an order of magnitude. Unfortunately, operation with these design changes initially resulted in no improvement in performance. Combining experimental observations and computer simulation, though, the group made several additional changes. Observation of current loss in the choke section led to the most important change: moving the left end of the cathode taper in Figure 7.35 to the right until it was located under the transition from the choke section to the MILO section. This improvement, in combination with the three others made at the outset, resulted in an increase in power to almost 2 GW and in pulse length to about 175 nsec, which was the length of the available power pulse, after factoring in the turn-on time of the device. However, experiments with the improved device showed that the pulse length and power were not

acceptably repeatable, and further computer simulation of the improved design with a shorter cathode showed that the problem was breakdown on the quarter-wavelength supporting stubs for the extractor and loss at the MILO end of the extractor. Further simulations pointed to a new design for the extractor supports and the velvet–metallic interface at the ends of the cathode; a shortening of the length of the cathode within the MITL load region to the minimum necessary to support the magnetic insulation current; a decrease in the inner diameter of the coaxial extractor to 19.30 cm; and an increase in the gap between the last MILO vane and the entrance to the coaxial region. In the absence of experiment, simulations pointed to a further power increase to 3.2 GW.

Subsequent increase of the pulsed power duration from 300 to 600 nsec revealed new issues in the generation of long pulses. Microwave emission would interrupt during the longer pulse, and then turn back on. Using a mix of experimental data and simulation, the problem was traced to a loss of insulation near the transition between the choke and MILO regions, even when the current exceeded the magnetic insulation threshold.[58,59] The magnetic insulation current is defined for unipolar electron flow, however, and simulations showed that the formation of anode plasma allowed the observed loss of insulation. The suggested fix was to shape the end of the cathode near the affected region to reduce the electric fields and electron flow there, thus reducing anode plasma formation.[57]

The other major thrust for MILO development has been motivated by a desire to address two fundamental MILO shortcomings: the energy lost to establishing the insulation current and the difficulty in extracting energy from the device when it operates in the π-mode with an axial group velocity that vanishes. In a first attempt to address this latter problem, a two-section device was designed, with an upstream section running in the π-mode, establishing the frequency and bunching the electrons appropriately, while the downstream section was an amplifier running in the π/2-mode with a positive group velocity.[60] Unfortunately, the improvements with this design were modest, first because the group velocity even for the π/2-mode was still rather small, and second because the downstream π/2-mode section was prone to break into oscillation at the somewhat different frequency of its own π-mode. The proposed improvement was the *tapered MILO* of Figure 7.37.[61]

The tapered MILO in the figure features an upstream three-cavity driver section that runs in its π-mode to bunch the electron flow and establish the operating frequency. In the reference, though, it was emphasized that the driver section is not just a prebuncher for the downstream tapered sections, since there is considerable additional electron emission from these sections. The group velocity in the gentle and sharp taper sections is increasing in order to propagate more microwave energy out of the device, without increasing the group velocity so quickly that the coupling between the drifting electrons and the structure is compromised. Placing the load diode within the device itself makes it possible to extract additional energy from the

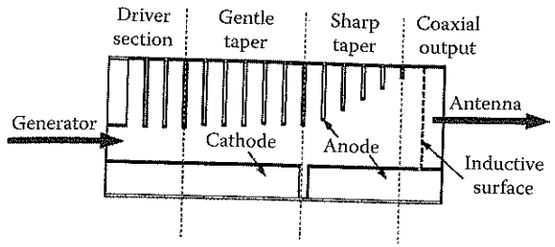

FIGURE 7.37
The tapered MILO. The central anode in this coaxial cylindrical geometry would be attached to the outer conductor by inductive posts. (From Eastwood, J.W. et al., *IEEE Trans. Plasma Sci.*, 26, 698, 1998. With permission.)

electron flow; tapping the energetic electron jets downstream of the gap contributes significantly to the output microwave power. Computer simulations and experiments indicate power levels in excess of 1 GW at efficiencies of 4 to 5%, although simulations also point to possible efficiencies well in excess of 10%.

The advantage of the MILO is its ability to operate at low impedance, so that high power can be achieved at relatively low voltage, particularly in large systems with anode and cathode radii that are close in value (a and b in the geometric factor G of Equation 7.37). MILOs thus couple effectively to low-impedance pulsed power drivers such as waterlines or explosive flux compression generators. Clark and coworkers at Sandia National Laboratories have operated MILOs at 0.72, 1.4, and 2.6 GHz.[62] Power levels in excess of a gigawatt and pulse lengths of hundreds of nanoseconds have been achieved. Breakdown and plasma generation leading to bipolar current loss from the slow-wave structures, as well as cathode jetting, have limited the pulse lengths. System design and construction are simplified by the fact that no external magnetic field coils are required.

The fundamental limitation of MILOs is their low efficiency, which can be traced to two factors. One is intrinsic to the system: the current that provides the insulating magnetic field is generated at high voltages, essentially equal to the operating voltage of the device. Thus, the penalty one pays for design simplicity in not having to provide separate magnetic field coils is the power required to generate the field with a high-voltage, high-current diode, since magnetic field is proportional to current, while power is equal to the product of current and voltage. The second factor contributing to low efficiency is the rather poor extraction efficiency for these devices. In part, this traces to the difficulty of axially extracting power from a device that tends to operate in the π-mode, where the group velocity vanishes. Radial extraction has been tried, but the results have been disappointing to date. The tapered MILO of Eastwood et al. in Figure 7.37 is designed to vary the group velocity at the end of the device in order to improve extraction. The location of the load diode within the MILO region itself is also aimed at recovering some of the energy in the magnetically insulated flow along the line.

Unfortunately, while Eastwood et al. estimate that as much as 40% of the input power is available to be converted to microwaves, and while simulations predict efficiencies in excess of 10%, experimentally measured efficiencies continue to be of the order of a few percent. Nevertheless, if one uses an energy-rich prime and pulsed power system based on explosive flux compression generators (see Sections 2.3 and 5.2.2) — providing adequate voltage and acceptably short rise times — the simplicity vs. efficiency trade may be acceptable. We note that the chemical energy density in high explosives is of the order of 4 MJ/kg.

7.8 Crossed-Field Amplifiers

For completeness, we briefly mention *crossed-field amplifiers* (CFAs). No true HPM version of this device has been successfully built, although one was designed with the intent of operating at 300 MW.[11] This cylindrical device was designed with a coaxial configuration like that originally due to Feinstein and Collier.[5] It was to be quite large, with an anode radius of just over 10.5 cm and 225 anode cavities. The operating mode was to be the $5\pi/6$-mode, and the gain was to be 17 to 20 dB, for a numerical gain of about 50 to 100, so that a master oscillator of 3 to 6 MW was going to be required to reach full power at the operating frequency of 11.4 GHz (see Problem 2).

7.9 Summary

Relativistic magnetrons have produced high power output at moderate efficiency from the L-band to the X-band: power levels of several gigawatts and efficiencies of 20 to 30% are achievable at the lower frequencies, and several hundred megawatts at several percent have been reached at the upper frequency. The technology is relatively mature, and the design of magnetron resonators is well understood: frequencies and modes of the cold resonator can be determined from well-known dispersion relations and fine-tuned for operation using computer simulation, while the experimental values of voltage and applied magnetic field are reasonably predicted by the Hull and Buneman–Hartree resonance conditions. The efficiency of relativistic magnetrons is intrinsically lower than that for nonrelativistic magnetrons; even so, the experimental efficiency of relativistic magnetrons is only about half their theoretical maximum. Consequently, anode erosion limits the lifetime — a problem that worsens as the frequency increases. Plasma evolved from the electrodes has been identified as a primary factor limiting pulse lengths, so that by addressing this issue, progress has been made in increasing the available energy per pulse at high power. In addition, the feasibility of operating relativistic magnetrons at repetition rates of at least a kilohertz has been demonstrated.

The generation of microwaves in magnetrons depends intrinsically on the radial flow of current to the anode, which in turn creates an axial drift of electrons out of the interaction region. Output power is thus fundamentally limited by a lower bound on magnetron impedance of a few tens of ohms. Therefore, further increases in power require either higher-voltage operation of single magnetrons or the phase-locked operation of multiple magnetrons. While this latter approach is by no means optimized, the principle has been demonstrated at several gigawatts.

The MILO promises very high power in a simplified configuration that eliminates the complication of adding separate magnet coils. In principle, one can scale the power up by building large-diameter cathodes, while retaining relatively small anode–cathode spacing. Methodical investigation of the causes of pulse shortening has allowed the extension of pulse lengths to several hundred nanoseconds. Unfortunately, efficiency has been limited to values well below 10%. Extraction is one limiting factor, but, perhaps more importantly, the fact that the insulating magnetic field is generated by current flowing at high voltage — the operating voltage of the device — is a fundamental limitation. Nevertheless, because of its simplicity of construction, robust operating mechanism, and low operating impedance, the MILO may be a good match for systems employing energy-rich, low-impedance explosive flux compression generators for their prime power.

Finally, high power CFAs have been designed for high power, but none have actually been operated.

Future developments in crossed-field devices will probably focus on pushing pulse durations toward a microsecond, mode control over the duration of such long pulses, repetitive operation, and phase locking of multiple units. The serious problem of efficiency in MILOs, as well as the less serious, but nevertheless challenging, problem of efficiency in magnetrons, will also be addressed.

Problems

1. Neglecting gap closure and the time dependence of the microwave source impedance, model a MILO as a constant 10-Ω impedance and a magnetron as a constant 100-Ω impedance. If each were driven by a pulsed power subsystem that could be modeled as a 1-MV voltage source in series with a pulsed power output resistance of Z_{PP}, plot the output power of the microwave source as a function of Z_{PP}.
2. If a CFA operating as an amplifier has a gain of 20 dB, how much input power is required to reach an output power of 1 GW?

3. In cylindrical magnetrons, as well as CFAs, the frequency is a function of the azimuthal mode number n.
   a. For such a magnetron with N anode cavities, what is the value of n if the device is operating in the π-mode?
   b. For a magnetron operating in the 2π-mode, what is the value of n?
4. a. If we design a CFA to operate in the 7π/12-mode, what is the minimum number of vanes, N, that it must have? What is the second-lowest possible number for N?
   b. What value of the mode number n corresponds to the 7π/12-mode for the minimum value of N? What value of n corresponds to the 7π/12-mode for the second-lowest value of N?
5. The frequency spacing between modes, $\Delta\omega_n$, is an important factor in ensuring stable operation in a given mode, designated by the mode number, n.
   a. How does $\Delta\omega_n$ vary with the number of anode vanes, N, for changes in the mode number, Δn, in the vicinity of the π-mode, which operates at frequency ω_π?
   b. How does $\Delta\omega_n$ vary with N for changes Δn in the vicinity of the 3π/2-mode, which operates at frequency $\omega_{3\pi/2}$?
6. Let us estimate the size of magnetrons of different frequencies between the L- and X-bands. Rather than perform the complicated calculation of deriving and solving a dispersion relation (such as that found in Section 4.4.2), proceed empirically with the data of Table 7.1 and Equation 7.3.
   a. Let $r_a = A\lambda$, with A a constant for all frequencies between 1 and 10 GHz. Justify the value of A you choose using the data in Table 7.1. (Note: You will have some latitude in your choice.)
   b. Use Equation 7.3 to estimate r_v (see Figure 7.1) for your values of r_a from part (a) for frequencies between 1 and 10 GHz.
   c. Estimate the length of the magnetron for frequencies between 1 and 10 GHz assuming a length $h = 0.9\lambda$.
   d. Assume that the azimuthal opening angle of the anode cavities is $\psi = 20°$ (see Figure 7.1) for N = 6 anode cavities. Further assume that the outer radius of the anode block is $r_b = r_v + 0.3$ cm. Compute an estimated mass for a stainless steel anode block (use a density for stainless steel of 7.9×10^3 kg/m^3).
7. a. If a magnetron of 1-GW output power operates at a power efficiency of 25%, and if all of the electrons emitted from the cathode strike the anode block, how much power is deposited in the block?
   b. If 20% of the electron current in the magnetron escapes axially, how much electrical power is deposited in the anode block?
8. What is the Hull field for magnetic insulation of an S-band magnetron operating at f = 2.8 GHz with $r_c = 1.26$ cm and $r_a = 2.1$ cm and an operating voltage of 700 kV? What is the Hull field of the magnetron if the voltage is raised to 1 MV?
9. Plot the Buneman–Hartree curve for an S-band magnetron operating at f = 2.8 GHz with $r_c = 1.26$ cm and $r_a = 2.1$ cm for voltages varying between 500 kV and 1 MV. Assume there is no axial current loss.
10. For the MIT A6 magnetron of Table 7.1 and Table 7.2, assuming a magnetic field of 1 T, what is the range of *possible* operating voltages defined by the Hull and Buneman–Hartree conditions? Assume no axial current loss.
11. The magnetron of Spang et al.[34] showed substantial frequency variation with variation of the cathode radius r_c when it operated in the 2π-mode, but relatively little frequency variation as r_c varied when it operated in the π-mode. Explain why, in qualitative terms.
12. An L-band magnetron operating at a 25-Ω impedance, driven by a 25-Ω Marx bank/waterline pulsed power driver, produces 3.6 GW when the open-circuit driving voltage of the pulsed power is 2 MV (so that the voltage across the magnetron is 1 MV). What is the efficiency of the magnetron? If the open-circuit pulsed power voltage is held constant at 2 MV, but a linear induction driver with a 75-Ω impedance is used, instead of the Marx bank/waterline system mentioned earlier, to what level does the output power drop if the magnetron impedance remains constant at 25 Ω? Assume the same efficiency.
13. Prove Equation 7.22.
14. a. For a coaxial MILO with an inner conductor radius of 5.7 cm and an outer conductor radius of 8.7 cm, plot the minimum insulating current, assuming the parapotential flow model of Equation 7.37 for voltages between 500 kV and 2 MV.
    b. For the same MILO, plot the parapotential impedance of the line Z_p over the same voltage range (500 kV to 2 MV).
    c. Estimate the drift velocity of the electrons in the line using Equation 7.38.
15. For a coaxial MILO with an inner conductor radius of 5.7 cm and an outer conductor radius of 8.7 cm, operating at a voltage of 700 kV, using the parapotential flow model of Equation 7.38, compute the drift velocity of the electrons in the line. For a line operating at a π-mode frequency of 2 GHz, estimate the spacing between vanes on the anode.
16. Consider the MILO of the previous problem, operating at a voltage of 700 kV. Assume that the inner line of the MILO is terminated in a flat cathode of circular shape that faces a flat anode. If the full

the emission of electron current from the cathode is uniform across the circular face at the space-charge-limited current density, what anode–cathode gap spacing is required in order for the current across the gap to equal the parapotential current for the line, I_p?

References

1. Boot, H.A.H. and Randall, J.T., The cavity magnetron, *IEEE Proc. Radiolocation Conv.*, 928, 1946.
2. Boot, H.A.H. and Randall, J.T., Historical notes on the cavity magnetron, *IEEE Trans. Electron Devices*, ED-23, 724, 1976.
3. Megaw, E.C.S., The high-power pulsed magnetron: a review of early developments, *IEEE Proc. Radiolocation Conv.*, 977, 1946.
4. Collins, J.B., *Microwave Magnetrons*, McGraw-Hill, New York, 1948.
5. Feinstein, J. and Collier, R., A class of waveguide-coupled slow-wave structures, *IRE Trans. Electron Devices*, 6, 9, 1959.
6. Okress, E., *Cross-Field Microwave Devices*, Academic Press, New York, 1961.
7. Bekefi, G. and Orzechowski, T., Giant microwave bursts emitted from a field-emission, relativistic-electron-beam magnetism, *Phys. Rev. Lett.*, 37, 379, 1976.
8. Palevsky, A. and Bekefi, G., Microwave emission from pulsed, relativistic e-beam diodes. II. The multiresonator magnetron, *Phys. Fluids*, 22, 986, 1979.
9. Clark, M.C., Marder, B.M., and Bacon, L.D., Magnetically insulated transmission line oscillator, *Appl. Phys. Lett.*, 52, 78, 1988.
10. Eastwood, J.W., Hawkins, K.C., and Hook, M.P., The tapered MILO, *IEEE Trans. Electron Devices*, 26, 698, 1998.
11. Eppley, K. and Ko, K., Design of a high power cross field amplifier at X band with an internally coupled waveguide, *Proc. SPIE*, 1407, 249, 1991 (available online from the Stanford Linear Accelerator Center SPIRES database: SLAC-PUB-5416).
12. Lau, Y.Y., *High-Power Microwave Sources*, Artech House, Boston, 1987, p. 309.
13. Lemke, R.W., Genoni, T.C., and Spencer, T.A., Three-dimensional particle-in-cell simulation study of a relativistic magnetron, *Phys. Plasmas*, 6, 603, 1999.
14. Treado, T., Generation and Diagnosis of Long- and Short-Pulse, High-Power Microwave Radiation from Relativistic Rising-Sun and A6 Magnetrons, Ph.D. thesis, University of North Carolina, Chapel Hill, 1989.
15. Kovalev, N.F. et al., High-power relativistic 3-cm magnetron, *Sov. Tech. Phys. Lett.*, 6, 197, 1980.
16. Smith, R.R. et al., Development and test of an L-band magnetron, *IEEE Trans. Plasma Sci.*, 19, 628, 1991.
17. Benford, J. et al., Variations on the relativistic magnetron, *IEEE Trans. Plasma Sci.*, PS-13, 538, 1985.
18. Lemke, R.W., Genoni, T.C., and Spencer, T.A., Investigation of rising-sun magnetrons operated at relativistic voltages using three-dimensional particle-in-cell simulation, *Phys. Plasmas*, 7, 706, 2000.
19. For a derivation of the relativistic Hull field and references to earlier derivations, see Lovelace, R.V. and Young, T.F.T., Relativistic Hartree condition for magnetrons: theory and comparison with experiments, *Phys. Fluids*, 28, 2450, 1985.
20. Benford, J., Relativistic magnetrons, in *High-Power Microwave Sources*, Granatstein, V.L. and Alexeff, I., Eds., Artech House, Boston, 1987, p. 351.
21. Price, D. and Benford, J.N., General scaling of pulse shortening in explosive-emission-driven microwave sources, *IEEE Trans. Plasma Sci.*, 26, 256, 1998.
22. Orzechowski, T.J. and Bekefi, G., Microwave emission from pulsed, relativistic e-beam diodes. I. The smooth-bore magnetron, *Phys. Fluids*, 22, 978, 1979.
23. Treado, T.A. et al., High-power, high efficiency, injection-locked, secondary-emission magnetron, *IEEE Trans. Plasma Sci.*, 20, 351, 1992.
24. Lopez, M.R. et al., Cathode effects on a relativistic magnetron driven by a microsecond e-beam accelerator, *IEEE Trans. Plasma Sci.*, 30, 947, 2002.
25. Craig, G., Pettibone, J., and Ensley, D., Symmetrically loaded relativistic magnetron, in *Abstracts for IEEE International Plasma Science Conference Record*, IEEE, Montreal, Canada, 1979.
26. Saveliev, Yu.M. et al., Effect of cathode end caps and a cathode emissive surface on relativistic magnetron operation, *IEEE Trans. Plasma Sci.*, 28, 478, 2000.
27. Phelps, D.A. et al., Rep-rate crossed-field HPM tube development at General Atomics, in *Proceedings of HPM 5*, West Point, NY, 1990, p. 169.
28. Sze, H. et al., Operating characteristics of a relativistic magnetron with a washer cathode, *IEEE Trans. Plasma Sci.*, PS-15, 327, 1987.
29. Ballard, W.P., Self, S.A., and Crawford, F.W., A relativistic magnetron with a thermionic cathode, *J. Appl. Phys.*, 53, 7580, 1982.
30. Kovalev, N.F. et al., Relativistic magnetron with diffraction coupling, *Sov. Tech. Phys. Lett.*, 3, 430, 1977.
31. Benford, J. and Sze, H., Magnetron research at Physics International Company, in *Proceedings of the 3rd National Conference on High-Power Microwave Technology for Defense Applications*, Kirtland AFB, Albuquerque, NM, 1986, p. 44.
32. Close, R.A., Palevsky, A., and Bekefi, G., Radiation measurements from an inverted relativistic magnetron, *J. Appl. Phys.*, 54, 7, 1983.
33. Smith, R.R. et al., Direct experimental observation of π-mode operation in a relativistic magnetron, *IEEE Trans. Plasma Sci.*, PS-16, 234, 1988.
34. Spang, S.T. et al., Relativistic magnetron repetitively pulsed portable HPM transmitter, *IEEE Trans. Plasma Sci.*, PS-18, 586, 1990.
35. Levine, J.S., Harteneck, B.D., and Price, H.D., Frequency agile relativistic magnetrons, *Proc. SPIE*, 2557, 74, 1995.
36. Arter, W. and Eastwood, J.W., Improving the performance of relativistic magnetrons, in *Digest of Technical Papers: International Workshop on High-Power Microwave Generation and Pulse Shortening*, Defence Evaluation and Research Agency, Malvern, U.K., 1997, p. 283.
37. Phelps, D.A. et al., Observations of a repeatable rep-rate IREB-HPM tube, in *Proceedings of the 7th International Conference on High-Power Particle Beams (BEAMS'88)*, 1988, p. 1347.
38. Vasil'yev, V.V. et al., Relativistic magnetron operating in the mode of a train of pulses, *Sov. Tech. Phys. Lett.*, 13, 762, 1987.
39. Ashby, S. et al., High peak and average power with an L-band relativistic magnetron on CLIA, *IEEE Trans. Plasma Sci.*, 20, 344, 1992.
40. Price, D., Levine, J.S., and Benford, J., Orion: A Frequency-Agile Field Test System, paper presented at the 7th National Conference on High-Power Microwave Technology, Laurel, MD, 1997.
41. Benford, J. and Benford, G., Survey of pulse shortening in high power microwave sources, *IEEE Trans. Plasma Sci.*, 25, 311, 1997.

42. Price, D., Levine, J.S., and Benford, J.N., Diode plasma effects on the microwave pulse length from relativistic magnetrons, *IEEE Trans. Plasma Sci.*, 26, 348, 1998.
43. Kerr, B.A. et al., Carbon velvet cathode implementation on the Orion relativistic magnetron, IEEE Pulsed Power Symposium, Basingstoke, UK, 2005, p. 6/1.
44. Treado, T. et al., Temporal study of long-pulse relativistic magnetron operation, *IEEE Trans. Plasma Sci.*, PS-18, 594, 1990.
45. Chen, S.C., Bekefi, G., and Temkin, R., Injection locking of a long-pulse relativistic magnetron, *Proc. SPIE*, 1407, 67, 1991.
46. Chen, S.C., Growth and frequency pushing effects on relativistic magnetron phase-locking, *Proc. SPIE*, 1226, 50, 1990.
47. Benford, J. et al., Phase locking of relativistic magnetrons, *Phys. Rev. Lett.*, 62, 969, 1989.
48. Woo, W. et al., Phase locking of high power microwave oscillators, *J. Appl. Phys.*, 65, 861, 1989.
49. Levine, J., Aiello, N., and Benford, J., Design of a compact phase-locked module of relativistic magnetrons, *Proc. SPIE*, 1226, 60, 1990; Levine, J. et al., Operational characteristics of a phase-locked module of relativistic magnetrons, *Proc. SPIE*, 1407, 74, 1991.
50. Fuks, M. and Schamiloglu, E., Rapid start of oscillations in a magnetron with a "transparent" cathode, *Phys. Rev. Lett.*, 96, 205101, 2005.
51. Black, W.M. et al., A hybrid inverted coaxial magnetron to generate gigawatts of pulsed microwave power, in *Technical Digest, 1979 International Electron Devices Meeting*, Washington, D.C., p. 175; Black, W.M. et al., A high power magnetron for air breakdown studies, in *Technical Digest, 1980 International Electron Devices Meeting*, Washington, D.C., p. 180.
52. Ballard, W.P., Private communication to Benford, J.N.
53. Vintizenko, I.I., Sulakshin, A.S., and Chernogalova, L.F., Generation of microsecond-range microwave pulses in an inverted relativistic magnetron, *Sov. Tech. Phys. Lett.*, 13, 256, 1987.
54. Slater, J., *Microwave Electronics*, Van Nostrand, Princeton, 1950, p. 309.
55. Creedon, J., Relativistic Brillouin flow in the high ν/γ limit, *J. Appl. Phys.*, 46, 2946, 1975.
56. Haworth, M.D. et al., Significant pulse-lengthening in a multigigawatt magnetically insulated transmission line oscillator, *IEEE Trans. Plasma Sci.*, 26, 312, 1998.
57. Calico, S.E. et al., Experimental and theoretical investigations of a magnetically insulated line oscillator (MILO), *Proc. SPIE*, 2557, 50, 1995.
58. Haworth, M.D., Luginsland, J.W., and Lemke, R.W., Evidence of a new pulse-shortening mechanism in a load-limited MILO, *IEEE Trans. Plasma Sci.*, 28, 511, 2000.
59. Haworth, M.D. et al., Improved electrostatic design for MILO cathodes, *IEEE Trans. Plasma Sci.*, 30, 992, 2002.
60. An unreferenced design by Ashby mentioned in the following reference.
61. Eastwood, J.W., Hawkins, K.C., and Hook, M.P., The tapered MILO, *IEEE Trans. Plasma Sci.*, 26, 698, 1998.
62. Clark, M.C., Marder, B.M., and Bacon, L.D., Magnetically insulated transmission line oscillator, *Appl. Phys. Lett.*, 52, 78, 1988.

8

BWOs, MWCGs, and O-Type Cerenkov Devices

8.1 Introduction

The general class of *O-type Cerenkov devices* includes the *relativistic backward wave oscillator* (BWO) and the *relativistic traveling wave tube* (TWT), higher-voltage and -current versions of the conventional BWO and TWT; the *multiwave Cerenkov generator* (MWCG), the highest power producer in this group, a large-cross-section device made possible by operation at relativistic voltages; and the *multiwave diffraction generator* (MWDG) and *relativistic diffraction generator* (RDG), large-cross-section devices capable of gigawatt-level operation at the X-band and above. This class of devices also includes the *dielectric Cerenkov maser* (DCM) and the *plasma Cerenkov maser* (PCM). For their operation, all of these devices depend on some type of *slow-wave structure* (SWS), which reduces the axial phase velocity of the microwaves within the device to a speed slightly below that of the beam electrons and less than the speed of light. Thus, the electrons radiate in these devices in a manner analogous to electrons emitting Cerenkov radiation when they travel through a medium at a speed greater than the local speed of light. They are called *O-type* devices because the electrons travel *along* the axial magnetic field that guides them through the device, rather than across the field, as in M-type devices such as the magnetron. Along with the magnetrons of Chapter 7, relativistic BWOs and MWCGs are the most mature of all high power microwave (HPM) sources, the relativistic BWO being the first true HPM source.

Representative source parameters for BWOs and the multiwave devices are shown in Table 8.1. For reasons that are perhaps more historic than physics based, these devices have been optimized for gigawatt-level power output from the S-band up to 60 GHz, with a peak power of 15 GW exiting the slow-wave structure of an MWCG at a frequency just below 10 GHz. All of the major devices in this class operate at an impedance around 100 Ω, so that voltages approaching, and exceeding, 1 MV are required for a microwave output in the gigawatt range. Output modes for the BWO and MWCG are usually TM_{01}, with an annular intensity pattern, unless a mode converter

TABLE 8.1

Representative Parameters for the O-Type Cerenkov Oscillators

Source Parameters	Sources		
	BWOs	MWCGs	MWDGs, RDGs
Frequency range	3–10 GHz	10–35 GHz	13–60 GHz
Peak power	3 GW	15 GW	4.5 GW
Electronic conversion efficiency	20%	48%	10–20%
Pulse width	~20 nsec	~100 nsec	Up to 700 nsec
Tunable range	300 MHz	150 MHz	NA
Repetition rate	200 Hz	NA	
Output mode	TM_{01}	TM_{01}	Complex
Bandwidth	~1%		
Voltage	0.5–1 MV	1–2 MV	1–2 MV
Electrical impedance	70–120 Ω	100–140 Ω	75–100 Ω
Magnetic field	3–4 T	~2.5 T	~2.8 T

is added downstream. The MWDG and RDG operate in higher-order radial modes with more complicated mode patterns. One of the TWTs with an internal mode converter had a plane-wave-like TE_{11} output.

MWCGs, MWDGs, and RDGs were all developed as large-cross-section devices, with diameters of a few to 10 wavelengths or more. Their strengths are large power production and long-duration/high-energy output pulses, but their large size and the mass and power demand of their magnetic field coils are drawbacks.

More compact BWOs have been optimized to operate in the S- and X-bands at several gigawatts and electrical efficiencies of 10 to 20%. Mechanical tunability in excess of 10% has been demonstrated. They have been taken into the field in a gigawatt-level radar, and they have been operated repetitively in the laboratory at up to 200 Hz with pulse lengths of 45 nsec. At the smaller resonator sizes for these systems, however, peak energy per pulse and average-power-handling capability are issues.

TWT amplifiers have received far less attention, but they have shown promising gains of about 35 to 45 dB, power levels of 400 MW to more than 1 GW, and efficiencies of 25% and more. However, issues of sideband control and uncontrolled oscillation have not yet been fully solved.

8.2 History

Rudolf Kompfner invented the TWT during World War II while working for the British tube establishment,[1] and the BWO followed immediately after the war. Some 25 years later, a BWO utilizing intense relativistic beam technology marked the beginning of the HPM era. It began in 1970 when John Nation of Cornell University used such a beam to generate an estimated 10 MW of microwaves at 0.05% efficiency.[2] Shortly thereafter, a team from the Lebedev Institute in Moscow and the Institute of Applied Physics in Nizhny Novgorod demonstrated the first true HPM source, a relativistic BWO that produced single 10-nsec, 400-MW pulses in the X-band.[3,4] A year after the publication of these results, a similar BWO at Cornell University raised the power to 500 MW,[5] and the race to produce ever-higher power levels using these devices was on. Further development split rather early into two primary lines of research. One led to a new class of devices that used large resonators to produce the highest powers and pulse energies, albeit at the expense of large size and power demand, while the other has continually improved the original BWO in a compact design that is nevertheless limited in pulse energy.

The former line of research involving the Russian Institute of High-Current Electronics (IHCE) in Tomsk, the Institute of Radio Engineering and Electronics (IREE) in Moscow, and Moscow State University pushed forward with a line of sources of increasingly higher power that began with the *surface wave oscillator* (SWO)[6] and *relativistic diffraction generator* (RDG).[7,8] Two modifications led to devices producing much higher output power:

- The use of larger, overmoded devices with diameters substantially greater than a wavelength increased the power-handling capacity of the initial SWO and RDG.
- The slow-wave structure was divided into bunching and output sections separated by a drift space of large enough radius that it was not cut off to the propagation of signal radiation.

The result was the MWCG[9] and the MWDG,[10] as well as two-section RDGs. The combination of these features in MWCGs, RDGs, and MWDGs driven by the powerful single-shot GAMMA accelerator[11] at IHCE — since taken out of service — led to the production of gigawatt power levels[12–14] at frequencies between 9 and 60 GHz. In the highest power experiment, an X-band MWCG coupled 15 GW into its output waveguide.

The second line of research, involving another group at IHCE and the Institute of Applied Physics, and later collaboration with the University of New Mexico and the University of Maryland, focused on improving the original BWO design. Continually improving the BWO, this grouping of institutes and universities has enhanced the efficiency through either axial variations in the slow-wave structure[15] or varying the location of the reflector at the input end of the device[16,17]; reduced the magnetic field at which the device operates[18]; and operated in a repetitive mode.[19] Coupled with one of the SINUS series of repetitive pulsed power machines, this device has powered gigawatt-class radars, including the NAGIRA system.[20,21] This combination could also be the basis for the RANETS-E mobile system that has been advertised as a co-development project for parties interested in a 500-MW microwave weapon.[22] In fact, we used it in the SuperSystem concept of Section 2.5.

Relativistic TWT amplifiers have received less attention than BWOs, in part because the properties of the driving electron beams make it difficult to avoid having the system break into oscillation. Nevertheless, X-band amplifiers of two very different designs have been developed at Cornell University, with the notable achievement of 45% efficiency at hundreds of megawatts output,[23] and at the Institute of Applied Physics (Nizhny Novgorod), with collaboration from the University of New Mexico, with a 45-dB gain at 1.1 GW in a TE_{11} output mode.[24] The master oscillator/power amplifier (MOPA) configuration, with a relativistic BWO driving a TWT amplifier, is more complex, but potentially more powerful in the aggregate. Researchers at Cornell demonstrated a BWO-driven, two-TWT array aimed at producing phase-locked output.[25]

Two types of devices use either a high-dielectric liner (the DCM) or a plasma (the PCM) within a smooth-walled waveguide as their slow-wave structure. From the 1970s through the 1990s, groups at Dartmouth College, the University of California at Irvine, Cornell University, the Tomsk Polytechnic Institute, and the Ecole Polytechnique in Palaiseau, France, produced moderately high powers with the DCM over a wide range of frequencies, notably 200 MW at 3.8 GHz,[26] 580 MW at 8.6 GHz,[27] and 1 MW at 75 GHz.[28] Since the mid-1970s, PCM investigations have largely been confined to the Institute of General Physics in Moscow, with a peak output of 300 MW.[29] In this book, we concentrate far less on DCMs and PCMs because we judge, in the former case, that metal slow-wave structures are more resistant to damage than dielectrics and, in the latter case, that a fixed structure provides greater control of slow-wave-structure properties than plasma.

8.3 Design Principles

The defining feature of Cerenkov devices is the use of a *slow-wave structure*. Consider Figure 8.1. When the phase velocity of the normal mode of the SWS equals that of the drifting electrons, each electron feels an accelerating or decelerating force, depending on the local phase of the wave. As a consequence, the beam bunches, but there is no net exchange of energy, because equal numbers of electrons speed up and slow down. If the electrons are initially somewhat faster than the wave, however, more electrons are decelerated than accelerated, and a resonant transfer of energy to the wave occurs in addition to the bunching. In devices of this type, the exchange of energy causes the wave to grow in amplitude, and the bunching enforces the coherence of the radiation.

Figure 8.2 shows the basic configuration of a Cerenkov device. An electron beam guided by a strong axial magnetic field is injected into a slow-wave structure, where the microwaves are generated; after passing through the

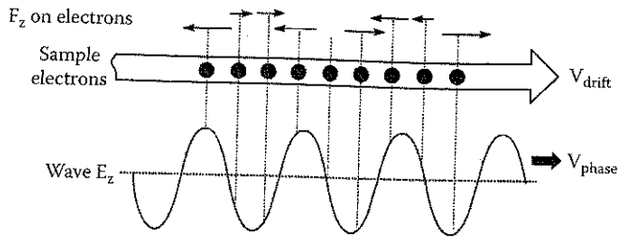

FIGURE 8.1
The bunching effect of the axial electric field of a slow wave on electrons in a beam.

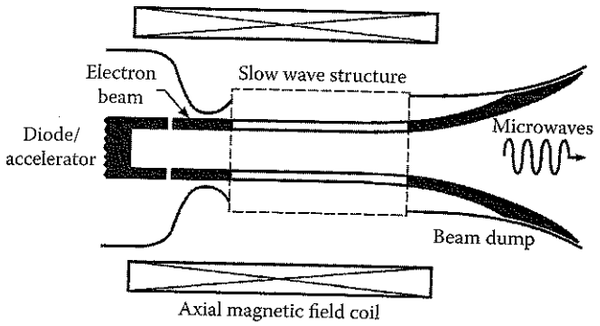

FIGURE 8.2
Basic configuration of the O-type Cerenkov devices. Examples of slow-wave structures are shown in Figure 8.3.

slow-wave structure, the beam flares to the wall in the beam dump. The key elements of these devices are:

- The electron beam, the energy source driving the generation of microwaves, which determines how much power is produced and, as we shall see, the pulse length to a large degree.
- The magnet producing the axial field that guides the beam through the device; this field can affect the output resonance and is a major contributor to system power demands and size and mass.
- The slow-wave structure, which enables the microwave-generating interaction and determines which of the many device types — BWO, MWCG, MWDG, etc. — one is designing, as well as the frequency, output mode structure, and ultimate power- and energy-handling capability. Figure 8.3 shows some examples of slow-wave structures.
- The beam dump, which is a driver for system cooling and x-ray shielding requirements, as described in Chapter 5. Also, if designed improperly, plasma evolved in the beam dump can travel along the axial field lines into the slow-wave structure and limit pulse lengths.

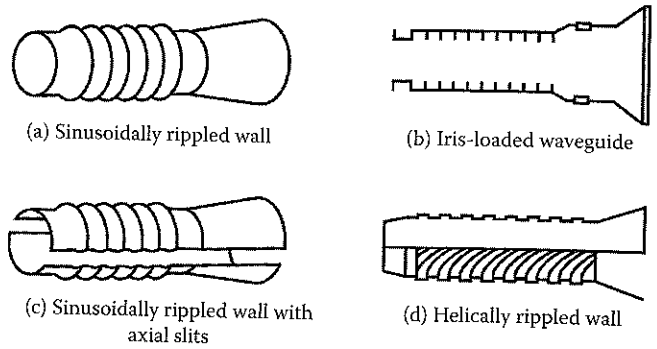

FIGURE 8.3
Examples of slow-wave structures. (From (b) Aleksandrov, A.F. et al., *Sov. Phys. Tech. Phys.*, 26, 997, 1981. With permission. (c) Zaitsev, N.I. et al., *Sov. Tech. Phys. Lett.*, 8, 395, 1982. With permission. (d) Bratman, V.L. et al., *IEEE Trans. Plasma Sci.*, 15, 2, 1987. With permission.)

In this section, we will consider the design relationships between the first three and the output parameters of a device.

The design process is outlined in Figure 8.4, with the shaded boxes at the right representing the main line of process flow:

- The first two steps are interrelated: to acceptable accuracy in these devices, we can treat the SWS and beam separately to estimate the potential operating frequencies and identify the device types (e.g., BWO, TWT, SWO, etc.) associated with each as a function of the transverse dimensions of the SWS and the parameters of the electron beam. Therefore, in Section 8.3.1 we treat the cold SWS in the absence of the beam, and in Section 8.3.2 we add the beam.
- The device types that we identify at the end of the second section fall into two basic classes: *oscillators*, which are by far the more prevalent, and *amplifiers*. For oscillators, there is a minimum beam current required for oscillations to start spontaneously; it is known as the start current, I_{st}. It depends on the mean radius and length of the SWS, the shape and dimensions of the perturbations of the wall, and the reflection coefficients at the ends. Obviously, it also depends on the beam parameters — current, electron energy, and transverse distribution; in some instances, the temporal pulse shape of the beam is also included. Finally, the strength of the magnetic field is significant, although it is usually strong enough that it is ignored unless the frequency of operation lies in a range where a cyclotron resonance competes with the Cerenkov mechanism. The start current is important in two regards. Clearly, the beam current must exceed this threshold for oscillator operation. Of equal importance, though, I_{st} provides a scale for the onset of nonlinear instabilities, which occur when the beam current exceeds some multiple of I_{st}. We treat these issues and the subject of gain in amplifiers in Section 8.3.3.

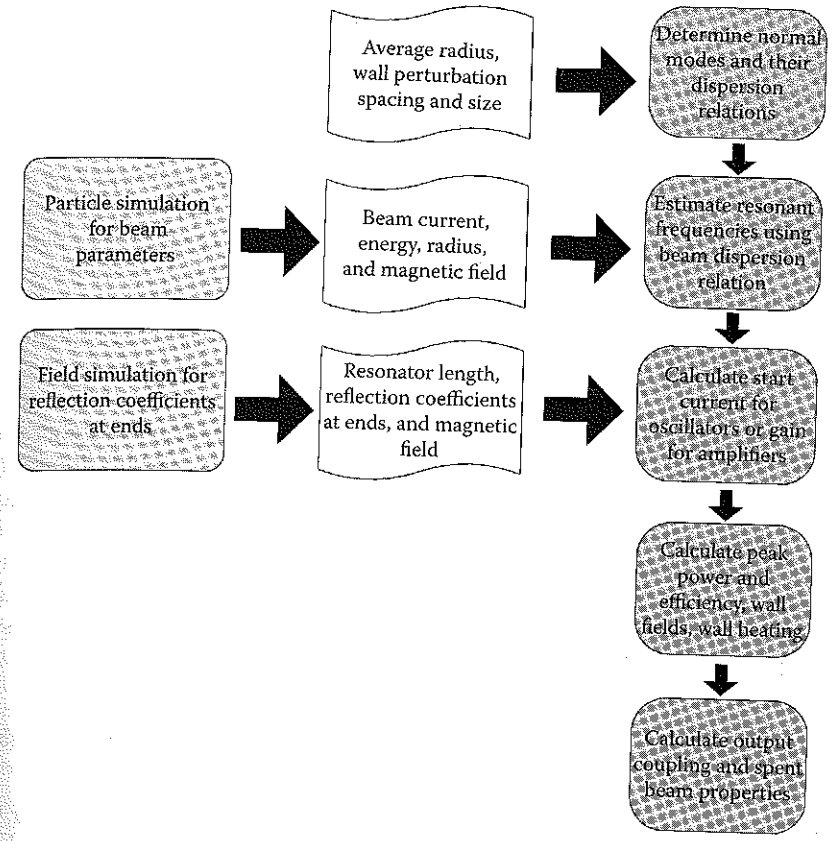

FIGURE 8.4
Basic design flow for O-type Cerenkov devices.

- The output power of oscillators and the linearity and ultimate saturation power of amplifiers are treated at the design stage using computer simulation and at the optimization stage by using computer simulation to augment, and help understand, the experiment. Wall fields and heating can be estimated using analytic estimates based on the understanding of the modes gained earlier. These subjects are all treated in Section 8.3.4.
- Output coupling in these devices is primarily limited to axial extraction of the microwaves through the beam dump. The output modes of BWOs and MWCGs are usually TM_{01}-like. Those for MWDGs and RDGs are more complex. At least one TWT has been designed to provide TE_{11} output.

O-type Cerenkov devices will operate at a resonance frequency and wavenumber, ω_0 and k_{z0}, found in the vicinity of the intersection between the dispersion curves for the SWS and those for the so-called *beam line*, $\omega = k_z v_b$. Understanding the dispersion properties of slow-wave structures is thus essential for (1) estimating operating frequencies, (2) calculating the dimensions of the SWS, (3) determining the output mode pattern, and (4) differentiating between the different O-type Cerenkov devices, as we shall see shortly. To a first approximation, the dispersion relationship for a slow-wave structure is actually quite close to that for a cold structure with no beam, so that the SWS and the beam can be treated separately. We therefore start by estimating the dispersion relation for the cold structure.

We discussed the dispersion relation for axially periodic slow-wave structures in Section 4.4.1 as part of our consideration of microwave-generating interactions. These structures are formed by periodically varying the radius of a waveguide, r_w; variations are typically axial, although as shown in Figure 8.3d, they can be helical as well. The two key features playing the dominant role in determining the frequency in O-type Cerenkov devices are the period of the variation in the wall radius, z_0, and the mean radius of the slow-wave structure, r_0. Restricting our attention to purely axial variations, the result of the periodic variation in the wall radius,

$$r_w(z) = r_w(z + z_0) \tag{8.1}$$

is that the radian frequency of the normal electromagnetic modes of the slow-wave structure ω is a periodic function of the axial wavenumber k_z:

$$\omega(k_z) = \omega(k_z + nh_0) = \omega(k_n) \tag{8.2}$$

where n is any integer, and

$$h_0 = \frac{2\pi}{z_0} \tag{8.3}$$

For most values of k_z, the detailed shape of the wall plays a secondary part in determining the shape of the curve of $\omega(k_z)$. Except near the points of intersection of the space harmonics of the smooth-walled-waveguide dispersion curves for the transverse magnetic (TM) modes, given, for example, by

$$\omega^2 = k_n^2 c^2 + \omega_{co}^2(0,p) \tag{8.4}$$

with

$$\omega_{co}(0,p) = \frac{\mu_{op} c}{r_0} \tag{8.5}$$

the dispersion curves for the slow-wave structure can be approximated by Equation 8.4. In Equation 8.5, μ_{op} is the pth root of the Bessel function J_o. Near the points of intersection for these curves, for different values of the indices n and p, though, the curves are modified in order to produce continuous, periodic curves for ω vs. k_z (see Problems 2 and 3).

To give an example, consider the slow-wave structure of Figure 8.5.[30] The variation of the dispersion relation for the lowest-order mode of the structure with the depth of the wall corrugation is shown in Figure 8.6. This particular curve is important because many, although not all, devices operate in this

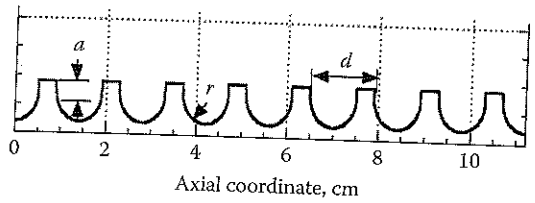

FIGURE 8.5
Wall radius profile for a BWO considered at the University of Maryland, with *r* the radius of a semicircular curve, *a* the depth of a rectangular portion of the wall figure, and *d* the notation for the periodicity of the wall variation in the reference. (From Vlasov, A.N. et al., *IEEE Trans. Plasma Sci.*, 28, 550, 2000. With permission.)

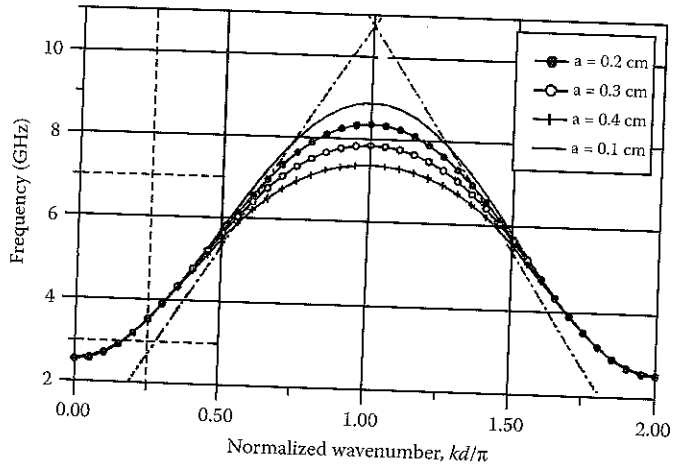

FIGURE 8.6
Calculated dispersion curve for the lowest-order TM_{01}-like mode of a slow-wave structure with a wall radius shaped as shown in Figure 8.5. The four curves correspond to four values of the parameter *a* in Figure 8.5, while *r* = 0.5 cm, *d* = 1.4 cm, and the distance from the axis to the nearest part of the wall is 4.2 cm. (From Vlasov, A.N. et al., *IEEE Trans. Plasma Sci.*, 28, 550, 2000. With permission.)

lowest-order mode. Note first that the plot is basically independent of the depth of corrugation over about one half of the curve, for k_z in the vicinity of 0 and $2\pi/z_0$. Secondly, we see that over the half of the curve surrounding the π point — where $k_z z_0 = \pi$ — the dispersion curve is increasingly depressed as the corrugation gets deeper. As a check on the estimate in Equation 8.4, consider the lower cutoff frequency for this band, where $k_z = 0$. The mean radius is $r_0 \approx$ 4.5 cm, taking account of the corrugation, so that Equations 8.4 and 8.5 yield $f(k_z = 0) = \omega_{co}/2\pi \approx 2.5$ GHz, which is just what we see in Figure 8.6. Next, consider the upper limit on the frequency for $k_z z_0 = \pi$, which we compute by setting $k_n = \pi/z_0$, to find $f_{max}(k_z = \pi/z_0) \approx 11$ GHz. We see that the wall corrugation drops the frequency considerably below this value, from something less than 9 GHz for a = 0.1 cm to about 7.3 GHz for a = 0.4 GHz. Summarizing, we see that r_0 determines the lower frequency in this passband, while z_0 plays a dominant role in determining the upper frequency. This situation becomes more complex for higher-order modes, though, in which case one must take account of neighboring modes and the exact connection between smooth-walled-waveguide modes in order to understand the mode dispersion curves.

Additional discussion of the dispersion relation for these devices is given in Section 4.4.1. As an additional point here, we remind the reader that the passbands for the different modes can overlap in frequency, although there is no crossing of dispersion curves for the different modes. In addition, we also remind the reader that the transverse variation of the electric and magnetic fields for a given slow-wave-structure mode can vary with k_z; these variations will resemble the smooth-walled-waveguide mode that best approximates the dispersion curve for a selected wavenumber, although the smooth-walled-waveguide mode can vary with k_z along a given slow-wave-structure dispersion curve.

8.3.2 Addition of the Beam: Resonant Interactions for Different Device Types

When we add the beam to the system, it enables the resonant interactions that create the microwave output. In this subsection, we discuss how to estimate the frequencies of these interactions and the types of devices (BWO, TWT, MWCG, etc.) that result.

In the absence of an electron beam, Maxwell's equations are linear, and the dispersion relation for the cold SWS is exact, subject to the approximation that it can be treated as if it were infinitely long. With the addition of the beam, the equations become nonlinear; we can proceed, though, under the assumption that the microwave signal is small enough that it weakly perturbs the beam, which allows us to determine the threshold for operation. The details of the dispersion relation for the coupled SWS–beam system depend on:

- The form of the wall radius axial variation, $r_w(z)$, which determines the shape of the cold slow-wave-structure dispersion curves of ω vs. k_z
- The value of the axial guiding magnetic field, which determines the degree to which electron cyclotron waves affect the beam–wave interaction
- The properties of the electron beam: its cross-sectional dimensions, current I_b, and electron kinetic energy, $(\gamma_b - 1)mc^2$, which determines the properties of the fast and slow space-charge waves* on the beam, which interact resonantly with the slow-wave-structure modes to generate microwaves through the transfer of electron kinetic energy to the electromagnetic fields

Expressions for the dispersion relation taking account of the slow-wave structure and the beam can be found in References 31 to 34.

The fast and slow space-charge waves on the beam have dispersion curves that are shifted upward and downward from the so-called beam lines given by (see Problems 4 and 5)

$$\omega = k_{n'} v_b = \left(k_z + n' h_0\right) v_b \tag{8.6}$$

The degree to which the space-charge wave dispersion curves of $\omega(k_z)$ are shifted above and below these lines (and the shifting is not symmetric for the two waves on the intense electron beams in HPM devices) depends on the current and voltage of the beam (see Problem 6). In the case of an effectively infinite axial magnetic field, for a thin annular-cross-section electron beam of mean radius r_b, the effect of the beam on the dispersion relation is through a term

$$\alpha \equiv \frac{\pi I_b}{\beta_b \gamma_b^3 I_A} \tag{8.7}$$

where $\beta_b = v_b/c$ is the normalized electron velocity and $I_A = 17.1$ kA. Note that α declines strongly in magnitude as γ_b increases, with a scaling like that for the so-called axial plasma frequency in a solid beam.

With no beam, the dispersion relation for the cold SWS allows only real values of ω when solved as a function of real k_z. When we include the beam, however, complex solutions for ω and k_z become possible. The waves grow in time if ω has a positive imaginary part, and in space if the real and imaginary parts of k_z have opposite signs. In general, the full determination of the complex values of ω and k_z depends on the boundary conditions at the ends of the SWS, but we defer that part of the problem to the next subsection.

* The terms *fast* and *slow* are sometimes a source of confusion, since both space-charge waves are slow in the sense of having phase velocities less than c. Better terms might have been *faster* and *slower*, but we bow to convention.

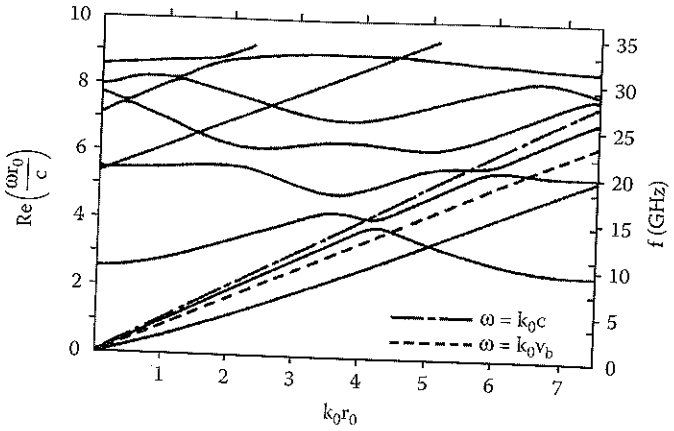

FIGURE 8.7
Dispersion diagram for a thin annular beam with I_b = 8 kA, γ_b = 1.91, and r_b = 0.5 cm, within a sinusoidally rippled-wall SWS with r_0 = 1.3 cm, r_1 = 0.1 cm, and z_0 = 1.1 cm. In keeping with the notation of the reference, k_0 corresponds to k_z in our notation. Dimensionless and dimensional values of the frequency are shown on the left and right sides, respectively. (From Swegle, J.A. et al., *Phys. Fluids*, 28, 2882, 1985. With permission.)

As an example of the effect of the beam, Figure 8.7 shows a plot of the solution to the dispersion relation for a slow-wave structure carrying a thin annular beam with I_b = 8 kA, γ_b = 1.91, and r_b = 0.5 cm; the SWS wall shape is given by

$$r_w(z) = r_0 + r_1 \sin(h_0 z) \tag{8.8}$$

with r_0 = 1.3 cm, r_1 = 0.1 cm, and $z_0 = 2\pi/h_0$ = 1.1 cm[33] (see Problem 1). In the plot, k_z is *assumed* to be real (although we emphasize that, in practice, we use the boundary conditions at the ends to complete the set of equations and determine the exact complex values of ω and k_z). Note the beam line in the figure, which actually is continued again at the left side of the plot at the frequency at which it passes off the plot on the right side. The fast and slow space-charge waves straddle the beam line. We see that the fast space-charge wave does not intersect the SWS dispersion curve; rather, one converts to the other as the wavenumber increases. The slow space-charge wave dispersion curve, on the other hand, does intersect the SWS dispersion curve. This is reflective of the fact that an unstable, microwave-generating interaction occurs in the vicinity of the intersection. Further, the curves do not actually intersect, because in Figure 8.7 we are only looking at a plot of the real part of ω vs. the wavenumber. If we examine the complex frequency, we find that it splits into complex conjugates, with opposite signs on the imaginary parts of ω. In Figure 8.8, we show the magnitude of the imaginary part of ω, which is known as the *growth rate* of the instability for real values of the wavenumber. We see that the wave is unstable only for a relatively

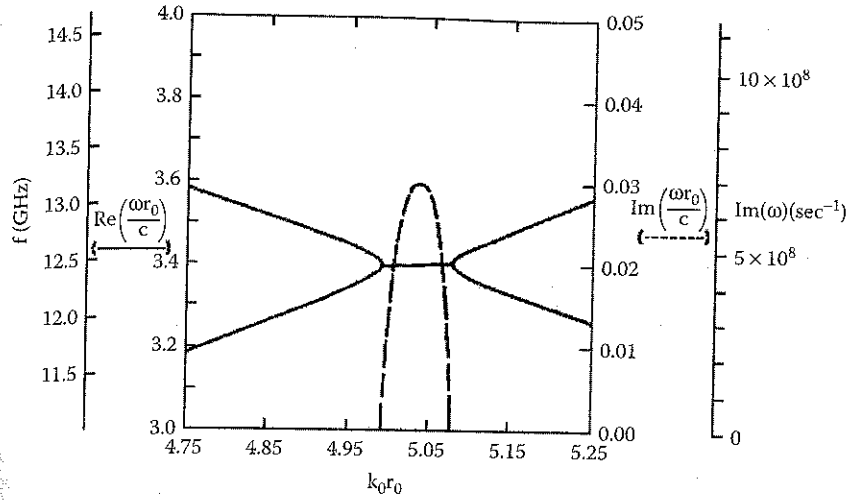

FIGURE 8.8
Detailed view of the real (solid line) and imaginary (dashed line) parts of ω near the lowest-order resonance in Figure 8.7. (From Swegle, J.A. et al., *Phys. Fluids*, 28, 2882, 1985. With permission.)

small range of frequencies in the neighborhood of the intersection between the slow space-charge wave and SWS dispersion curves. Similarly unstable behavior is seen near the intersections at higher frequencies, although the growth rates decline as the real part of the frequency increases.

The operating frequencies, electromagnetic modes, and device types can be determined approximately by finding the intersections between the slow space-charge waves on the beam — with dispersion curves that are usually well approximated by Equation 8.6 — and the cold SWS modes discussed in the previous section. *The different device types — BWOs, TWTs, SWOs, and so on — are distinguished primarily by the slope of the slow-wave-structure dispersion curve at these resonant intersections.* The slope of the SWS curve is the group velocity, $v_g = \partial\omega / \partial k_z$, which is the speed of axial transport of energy by the structure mode. To see how we distinguish the different device types, consider the three example beam lines treated in Figure 8.9, each for a beam of different axial velocity. First, the lowest-velocity beam line in the figure ($v_b = v_{z1}$) intersects the lowest-frequency structure mode at point 1 (BWO), where $v_g < 0$. This is a BWO interaction, and the *backward wave* designation stems from the fact that the structure mode carries energy backward, against the direction of the beam velocity. The same beam line intersects the next higher frequency structure mode at point 2 (TWT), where $v_g > 0$ for the structure. The interaction at this resonance could be exploited to build a TWT, in which the SWS transports electromagnetic energy *forward*.

The dashed beam line in the figure ($v_b = v_{z2}$) intersects the second passband at point 3 (RDG), where $k_z = h_0$. Relativistic diffraction generators are defined

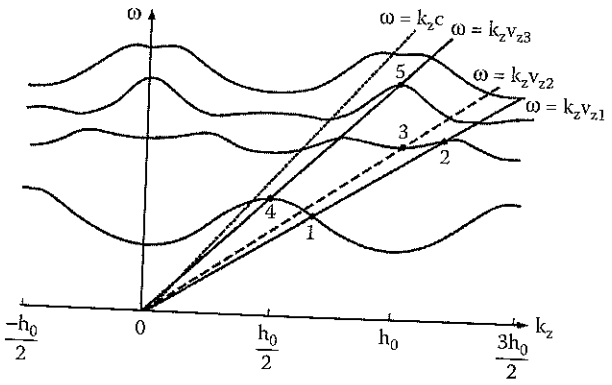

FIGURE 8.9
Example beam lines for three different beams with axial beam velocities $v_{z1} < v_{z2} < v_{z3}$, and their resonances with the slow-wave-structure dispersion curves. Of the intersections (resonances) singled out, 1 is a BWO, 2 is a TWT, 3 is an RDG, 4 is an SWO, and 5 is a Wood's Anomaly (WA). Note that 4 lies below the light line, $\omega = k_z c$.

by these intersections at points where $v_g = 0$ for the SWS mode, except for the special resonance marked point 4 (SWO), to which we return in a moment. The particular RDG resonant chosen in this figure would in fact allow operation in the *2π-mode*, because the wave phase shift from one SWS section to the next, separated by a distance z_0, is $k_z z_0 = 2\pi$.

At higher beam energies, with $v_b = v_{z3}$, the beam line intersects the lowest passband mode at "SWO." This intersection for *π-mode* operation (i.e., $k_z z_0 = \pi$) can occur for both n and n′ equal to 0 in Equations 8.4 and 8.6 *only if* the top of the lowest passband lies below the *light line*, $\omega = k_z c$. In this event, the axial electric field will have the character of a *surface wave*, with its amplitude peaking close to the walls of the structure, and evanescently dropping off toward the interior.* Operation at the resonance marked "SWO" thus results in a surface wave oscillator. Qualitatively, to achieve SWO operation, the ripple amplitude must be sufficiently large to depress the peak of the lowest dispersion curve below the light line. The derivations[31,35] for a sinusoidally rippled SWS (Equation 8.8) show that the peak of the lowest dispersion curve lies below the light line in the event that

$$r_1 > 0.3\frac{z_0^2}{r_0} \tag{8.9}$$

when $r_0^2 >> 0.6z_0^2$.

* To see this important fact, one must solve Maxwell's equations for the form of the axial field in the SWS, and then the dispersion relation to show that when $\omega < k_z c$, the primary contribution to that field component is described by the I_0 Bessel function, which grows with radius approximately as $\exp(k_\perp r)$.

Finally, the beam line for $v_b = v_{z3}$ intersects the third SWS dispersion curve at point 5 (WA). This is a higher-order 2π-mode that will also support RDG operation, but it differs qualitatively from the 2π-mode at the point marked "RDG" because "WA" is a special point on the dispersion curve referred to in the literature as Wood's anomaly. At this point, the SWS dispersion curve results from the intersection of two smooth-wall TM_{01} dispersion curves given by Equation 8.4 with n = 0 and n = –2, and p = 1 for both. In contrast, the point marked "RDG" results from the n = –1 spatial harmonic of the TM_{02} mode near cutoff [i.e., $\omega \approx \omega_{co}(0, 2)$]. Since the SWS curve at "WA" lies below the light line, the mode in question is a surface wave mode, akin to the fields associated with "SWO," rather than a volume wave mode, like the fields associated with "RDG" for $v_0 = v_{z2}$. The efficiency of converting beam energy to diffraction radiation is enhanced at this point,[36] so that it becomes advantageous to operate RDGs.

The multiwave devices, the MWCG and the MWDG, are distinguished from the other devices, first, by the fact that they have overmoded slow-wave structures (i.e., they are several or more wavelengths in diameter) and, second, by the fact that their slow-wave structures are sectioned, with at least two sections separated by a drift space that is *not* cut off to propagation between sections.* In the particular case of the MWCG, the individual sections of the composite SWS have dispersion curves like those for SWOs. In the MWDG, on the other hand, the individual sections are different, so that, for example,[10] the first has the character of a BWO (beam–SWS intersection with $v_g < 0$), while the second has that of an RDG ($v_g = 0$) in the 3π/2-mode.

The sign of v_g at resonance has a fundamental effect on the character of the associated device. When $v_g < 0$, as it is in BWOs, there is an intrinsic feedback mechanism that makes the device act as an oscillator with no driving signal required, provided the beam current exceeds a threshold known as the *start current*, I_{st}, which we will discuss in the next subsection. For those devices where $v_g = 0$ at resonance — SWOs, MWCGs, RDGs, and MWDGs — the SWS effectively becomes a high Q resonator because the electromagnetic energy does not convect through the system (i.e., the situation is akin to the establishment of a standing wave pattern in the SWS, albeit modified by power extraction from the end). Therefore, these devices also operate almost exclusively as oscillators, provided $I_b > I_{st}$.

When $v_g > 0$, energy tends to convect downstream, so that an ideal device with no end reflections will operate as a TWT amplifier for an upstream input signal. Let us emphasize the word *ideal* in connection with amplifiers. In real devices of this type, two nonideal factors modify the situation: (1) given the very high gain associated with the intense electron beam driver, many times noise is spontaneously amplified in a *superradiant* mode of operation; or (2) reflections from the downstream end of the device can provide sufficient feedback that the TWT will break into oscillation above

* We emphasize that the intermediate sections are not cut off, so that this arrangement is not confused with the historical practice of *severing* slow-wave structures with cutoff drift sections.

some threshold current. The challenge in designing amplifiers is thus to avoid spontaneous oscillation while obtaining high gain, defined as the ratio of output microwave power, P_{out}, to the input signal power, P_{in}, by

$$P_{out} = GP_{in} \tag{8.10}$$

As we can see, there is a large — in fact, infinite — number of resonances available for microwave generation. A variety of techniques can be applied to make one resonance take precedence over the others in order to generate a clean, single-frequency signal at the maximum possible power. We refer to this as *mode selection*. In many cases, the modes at the lowest frequencies tend to dominate; the first relativistic BWO operated at the lowest, TM_{01}-like resonance,[3] while in the Cornell experiments published a year later,[5] delay-line diagnostics detected power in the two lowest modes on the same pulse. This tendency can be overcome. As we mentioned, when $v_g \approx 0$ at resonance, as it does in SWOs, MWCGs, RDGs, and MWDGs, the slow-wave structure behaves as a high Q resonator, allowing the preferential selection of these resonant modes.[37] Two further examples involve (1) carefully choosing the beam radius and using cyclotron resonance absorption of unwanted mode energy[38] to select TM_{02} operation over TM_{01}, and (2) cutting long slits on either side of a resonator to select modes with azimuthal field variations.[39]

8.3.3 Start Current and Gain

Let us first consider the start current for oscillations, I_{st}. The calculation of I_{st} is quite involved, and the references provide detailed calculations for a number of specific situations:

- BWOs operating at low currents, for which the scaling term from Equation 8.7 is $\alpha^{1/3} << 1$, with an infinite magnetic field and with simplified boundary conditions of perfect wave reflection at the beam input end of the SWS and perfect wave transmission at the beam output end[35,40,41]
- BWOs with infinite magnetic fields and general reflection coefficients at the ends[42,43]
- BWOs with finite magnetic fields operating near cyclotron resonance with general reflection coefficients[44]
- SWOs with infinite magnetic fields and general reflection coefficients[37]

We will not detail those calculations, which are beyond the scope of our presentation, but it is valuable to understand the underlying concept. The dispersion relation provides a single relationship between ω and k_z that does not allow us to fully specify them both. In fact, for a device operating at a

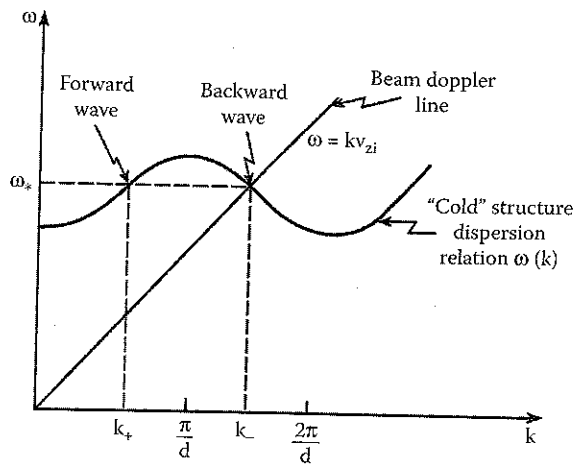

FIGURE 8.10
Schematic depiction of the resonant interaction at $k_z = k_-$ between the lowest-order TM_{01}-like slow-wave-structure mode, a backward wave, and the beam mode, as well as the forward-directed wave at the same frequency as the resonance but with wavenumber k_+. (From Levush, B. et al., *IEEE Trans. Plasma Sci.*, 20, 263, 1992. With permission.)

fixed frequency corresponding to one of the beam–SWS resonances, there are several other nonresonant modes (i.e., away from the intersection of the beam and SWS curves) with the same ω but different values of k_z that will be linearly coupled to the resonant mode by the reflection coefficients at the ends. To take an example, consider Figure 8.10.[42] In the coupled-mode treatment, the resonant BWO mode couples to a forward-directed mode with the same ω but different k_z. By using the boundary conditions at the two ends of the finite-length SWS in conjunction with the dispersion relation for the SWS, one now has three conditions in the three unknowns of ω, k_+, and k_-. In general, all three quantities are complex, and the start current is the minimum value of I_b for which waves grow in time. In other words, when the temporal behavior of quantities is of the form $\exp(i\omega t)$, the imaginary part of ω is positive for $I_b < I_{st}$ and negative (with exponential wave growth) for $I_b > I_{st}$.

As the beam current increases beyond I_{st}, it becomes apparent that there is in fact a hierarchy of start currents.[35] At the lowest value, call it I_{st1}, one axial mode with an axial structure defined by the sum of waves, each with its own value of k_z, oscillates. Above a second, larger value, call it I_{st2}, a second mode with a slightly different frequency and axial mode structure joins the first. A third mode of different frequency and mode structure joins the first two above I_{st3}, and so on as I_b increases. Under the rather restrictive assumptions of Swegle[35] — low current, infinite magnetic field, and idealized end conditions — $I_{st2} = 6.63I_{st1}$ and $I_{st3} = 14.4I_{st1}$.

When one includes general values of the reflection coefficients at the ends of the SWS, the start current is found to be a periodic function of resonator length, L. In particular, when reflections at the output end are added to the

calculation, the start current is usually reduced from the idealized value found under the assumption of perfect transmission there, although there are ranges of L for which interference between the coupled waves in the interaction region actually increases I_{st}. Because of the high Q nature of their resonators, start currents are generally lower in SWOs than in BWOs. Overall, start currents are increased when one takes account of the actual time dependence of I_b and γ_b, rather than assuming constant values for each.

For the finite values of the magnetic field, the behavior of I_{st} and device operation overall are modified significantly by the competition between the Cerenkov growth mechanism and absorption by spatial harmonics of the fast cyclotron wave.[44] The effect is most pronounced in the vicinity of the resonant magnetic field value, B_{res}, defined as the field at which the (–1)st spatial harmonic of the fast cyclotron wave resonates with the SWS at the same frequency as the Cerenkov resonance, so that the two compete. Thus, if ω_0 and k_{z0} are the values of frequency and wavenumber at the Cerenkov resonance between the SWS and the beam, then

$$\omega_0 \approx \left(k_{z0} - h_0\right)v_b + \Omega_c = \left(k_{z0} - h_0\right)v_b + \frac{eB_{res}}{m\gamma_b} \tag{8.11}$$

Since the Cerenkov resonance occurs where the beam line of Equation 8.6 is $n' = 0$, B_{res} is given by

$$B_{res} \approx \frac{2\pi m\gamma_b v_b}{ez_0} \tag{8.12}$$

The situation for magnetic fields at or near resonance is rather complicated, but generally I_{st} is increased, the stability of the interaction at larger currents is affected, and under some circumstances cyclotron absorption can make device operation impossible. Note also that resonances with higher-order spatial harmonics of the fast cyclotron frequency are possible, so that there are resonant field values at multiples of the value in Equation 8.12.

Although I_b must exceed I_{st} in order for an oscillator to operate, it is possible to have too much of a good thing. Levush et al.,[42] using a formalism and assumptions different from those of Swegle,[35] show that two nonlinear instabilities will modify, and in many cases degrade, the output behavior of a BWO for I_b appreciably above I_{st}. Figure 8.11 is a map of the regions of instability in a two-dimensional parameter space of dimensionless variables; the normalized length on the horizontal axis is the actual SWS length L divided by v_b/ω_0, with ω_0 the operating frequency, while the vertical axis is proportional to the length of the system and the beam current divided by the cube of $N = L/z_0$.* For the plot, the following parameters are fixed: (1) the

* The normalization parameter for I_b is rather complex, and in the interest of brevity, we refer the reader to Levush et al.[42] for details.

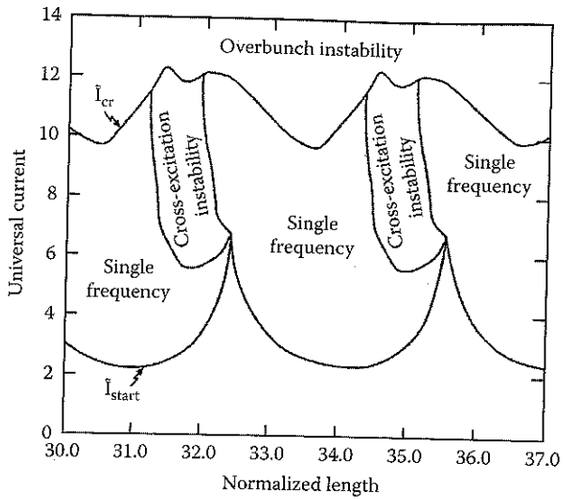

FIGURE 8.11
Regions of BWO operation in a space of normalized device current and normalized device length, assuming a combined reflection coefficient of 0.7 at the two ends of the device. (From Levush, B. et al., *IEEE Trans. Plasma Sci.*, 20, 263, 1992. With permission.)

product of magnitudes of the complex reflection coefficients at the ends, (2) v_b, and (3) the group velocity of the slow-wave-structure wave at resonance. Note that there are regions where one expects (1) single-frequency operation, (2) the *cross-excitation instability*, or (3) the *overbunch instability*.

The cross-excitation instability parameter space extends upward from the cusps in the lower boundary of the single-frequency region for values of $I_b > I_{st}$. On physical grounds, this happens because those cusps reflect rapid changes in I_{st} as the system shifts from one lowest-order axial mode to the next as the normalized length, $L\omega_0/v_b$, increases. This instability results from a nonlinear reduction in the start current for a competing axial mode in the vicinity of this region where axial modes shift. It manifests itself as shown in Figure 8.12, where the system begins oscillating in a lower-frequency mode, later jumping to a slightly *higher* frequency in a different axial mode; note that in a sense, system performance is improved by the higher-power operation in the latter mode. This instability has been observed experimentally.[45]

The overbunch instability, on the other hand, is a nonlinear effect resulting from the very strong beam bunching that occurs when I_b is substantially larger than I_{st}; this leads to operation in the primary mode as well as a sideband *downshifted* in frequency (similar to behavior observed in klystrons and other O-type sources). This sideband strongly modulates the output signal. Levush et al.[42] note that for much larger currents, with $I_b \sim 30I_{st}$, the microwave fields become so large that electron velocities are actually reversed.

As a rule of thumb, to avoid nonlinear instabilities that create mode hopping and sideband formation, it is desirable to operate an oscillator of this